J. Fluid Mech. (1995), *vol.* 297, *pp.* 101–122

Boundary-layer transition triggered by hairpin eddies at subcritical Reynolds numbers

By MASAHITO ASAI[1] AND MICHIO NISHIOKA[2]

[1] Department of Aerospace Engineering, Tokyo Metropolitan Institute of Technology, Asahigaoka 6-6, Hino, Tokyo 191, Japan

[2] Department of Aerospace Engineering, University of Osaka Prefecture, Gakuencho 1-1, Sakai, Osaka 593, Japan

(Received 18 February 1994 and in revised form 4 April 1995)

Subcritical transition in a flat-plate boundary layer is examined experimentally through observing its nonlinear response to energetic hairpin eddies acoustically excited at the leading edge of the boundary-layer plate. When disturbed by the hairpin eddies convecting from the leading edge, the near-wall flow develops local three-dimensional wall shear layers with streamwise vortices. Such local wall shear layers also evolve into hairpin eddies in succession to lead to the subcritical transition beyond the x-Reynolds number $R_x = 3.9 \times 10^4$, where the momentum thickness Reynolds number R_θ is 127 for laminar Blasius flow without excitation, and is about 150 under the excitation of energetic hairpin eddies. It is found that in terms of u- and v-fluctuations, the intensity of the near-wall activity at this critical station is of almost the same order as or slightly less than that of the developed wall turbulence. The development of wall turbulence structure in this transition is also examined.

1. Introduction

Laminar to turbulent transition in a boundary layer strongly depends on the disturbance environment. Under low background turbulence, transition in Blasius flow is initiated with the spatial (convective) growth of viscosity-conditioned Tollmien–Schlichting waves at Reynolds numbers far beyond the critical value for the linear instability. A number of laboratory and numerical experiments have documented the process by which the wave growth leads to the breakdown into wall turbulence through a sequence of flow instabilities, i.e. the secondary instability (see the reviews by Herbert 1988; Bayly, Orszag & Herbert 1988; Kachanov 1994), the high-frequency secondary (or tertiary) instability (Klebanoff, Tidstrom & Sargent 1962; Kovasznay, Komoda & Vasudeva 1963; Hama & Nutant 1963; Nishioka, Asai & Iida 1980) and the final breakdown of near-wall shear layers (Nishioka, Asai & Iida 1981; Nishioka & Asai 1984; Fasel 1990; Sandham & Kleiser 1992). In contrast to the well-documented transition under a low turbulence level, we have little information on the possible subcritical boundary-layer transition due to high-intensity (nonlinear) disturbances. Our knowledge on the response of a boundary layer to nonlinear strong disturbances at subcritical Reynolds numbers is crucial in understanding, for example, the attachment-line contamination on a swept wing (e.g. Gaster 1967; Poll 1979).

In plane Poiseuille flow which has almost the same instability and transition characteristics as Blasius flow (Nishioka, Iida & Ichikawa 1975; Nishioka *et al.* 1980; Asai & Nishioka 1989), the subcritical transition can be observed at Reynolds numbers of around 1000 (based on the channel half-depth and the centreplane velocity) when

the inlet flow is highly disturbed; see Carlson, Widnall & Peeters (1982) and Nishioka & Asai (1985). Experiments by Henningson & Alfredsson (1987) and Klingmann (1992) and numerical simulations by Henningson & Kim (1991) also reveal that a turbulent spot may develop from localized nonlinear disturbances at such low Reynolds numbers. Thus, the Reynolds number for possible transition in plane Poiseuille flow is lower than the critical Reynolds number for the linear instability 5772 (Orszag 1971). More importantly, the minimum transition Reynolds number in plane Poiseuille flow is about 130 and 330 in terms of the Reynolds number based on the momentum thickness and displacement thickness respectively. So, since the critical Reynolds number calculated from the linear stability theory (the parallel-flow theory) for Blasius flow is respectively 200 and 520 (based on the momentum thickness and displacement thickness respectively), there is a high possibility of the occurrence of subcritical transition in Blasius flow too. Indeed, Morkovin (1988) reported that a turbulent wedge developing from an isolated roughness may grow with the occurrence of wall burst around the critical Reynolds number for the linear instability.

According to our previous study on ribbon-induced transition in plane Poiseuille flow (Nishioka *et al.* 1981; Nishioka & Asai 1984), at the later stage of the high-frequency secondary instability (or the multi-spike stage) intense shear layers developed close to the wall, being associated with the passage of hairpin eddies (which successively developed from the high-shear layer away from the wall) and then the wall shear layers themselves seemed to evolve into hairpin eddies. At that stage, the mean flow exhibited a log-law velocity distribution, so the almost periodic flow we observed was judged to be very close to the turbulent stage. In the present experiment on the subcritical transition in Blasius flow, we try to realize the flow stages similar to the spike stages, near the leading edge of a boundary-layer plate, by applying a periodic acoustic forcing. This approach also enables us to obtain much information on the mechanism of wall turbulence generation through observing the wall turbulence structures when they first appear.

The successive occurrence of hairpin-shaped vortices from the wall shear layer has also been observed in the growth process of a turbulent spot. For instance, Matsui's (1980) experiment on the development of a turbulent spot clearly showed that the successive generation of hairpin eddies leads to the growth of the spot. Acarlar & Smith (1987*a*, *b*) examined the response of the boundary layer to hairpin eddies developing from a hemisphere on the wall by using flow visualization techniques, and suggested that the successive growth of hairpin eddies was responsible for the wall turbulence generation. The regeneration process of hairpin eddies was also examined in detail by Smith *et al.* (1991) and Haidari & Smith (1994).

In the following, we investigate the response of a flat-plate boundary layer to energetic hairpin eddies excited at the leading edge to clarify the possibility of the subcritical transition and the related critical condition. Some preliminary results of the present experiment were presented briefly in Asai & Nishioka (1990).

2. Experimental set-up and procedure

The experiment is conducted in a wind tunnel with an open jet, 200 mm × 200 mm in cross-section. A schematic of the test section is illustrated in figure 1. A flat plate set in the test section is 600 mm long, 3 mm thick and 195 mm in span, and has a sharp leading edge. A pair of large plexiglas sidewalls maintain the two-dimensionality of the mainstream. To excite vortices at the leading edge acoustically, a loudspeaker with a 30 cm woofer is used. The forcing current is supplied by a sine-wave generator through

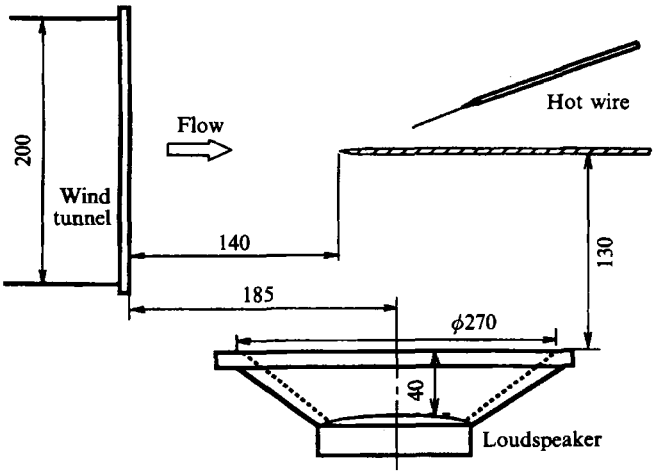

FIGURE 1. Schematic of the test section (dimensions in mm).

a power amplifier. The sound is radiated almost perpendicularly to the boundary-layer plate, and therefore can cause local unsteady flow separation at the sharp leading edge to excite discrete vortices there, as will be shown in detail in the next section. It should be noted that the areas above and below the plate are open to avoid possible acoustic resonance. As will also be seen in the next section, thin plastic tapes of 0.05 mm thick and 3 mm wide are glued around the leading edge every 6 mm in the spanwise direction, to control the three-dimensional distortion of the discrete vortices excited. The coordinate system is as follows: the x-axis is in the streamwise direction (measured from the leading edge), the y-axis is normal to the upper surface of the plate and the z-axis is in the spanwise direction.

A constant-temperature hot-wire anemometer (with linearizer) is used to measure the time-mean and fluctuation velocities in the x-direction, U and u. The sensitive length of the hot wire (a tungsten wire of 5 μm in diameter) is 1 mm. The hot-wire probe can be traversed in the three (x, y and z) directions continuously. The y-distributions of the mean velocity $U(y)$ and the r.m.s. value $u'(y)$ are simultaneously recorded on an XY recorder during each y-traverse. The hot-wire signal is stored in a data recorder. Flow visualizations are done by means of the smoke-wire technique to identify the three-dimensional flow structures. The smoke wire (or wires), stretched in the spanwise (z) direction, can be traversed in the x- and y-directions, and the cross-section view of the smoke pattern is made using a sheet of stroboscopic light. The visualization pictures are recorded by still camera shots (synchronized with the forcing signal) or a high-speed camera.

The free-stream velocity U_∞ is fixed at 4 m s^{-1}. We measured carefully the time-mean velocity distributions $U(y)$ at various x-stations in the laminar boundary layer without the acoustic forcing, and confirmed that Blasius flow developed from the vicinity of the leading edge, as seen from figure 2 which compares the measurement of the mean velocity $U(y)$ at each x-station with the corresponding Blasius profile. At $x = 300$ and 440 mm, the Reynolds number based on the displacement thickness R_L^* (the subscript L stands for the laminar flow without the forcing) is about 500 and 600 respectively. The critical R_L^* given by the Orr–Sommerfeld stability equation is 520. Note that according to the direct numerical simulation by Fasel & Konzelmann (1990) and the PSE (parabolized stability equations) calculation by Bertolotti, Herbert & Spalart

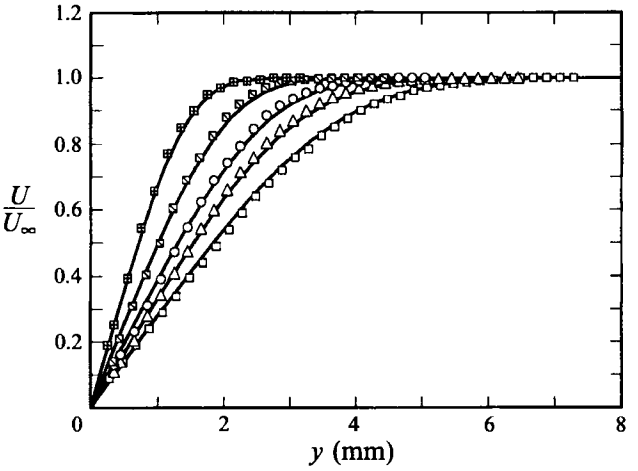

FIGURE 2. The y-distributions of mean velocity U at $x = 60$ mm (⊞), 120 mm (⊠), 200 mm (○), 280 mm (△) and 400 mm (□). Solid curves represent the corresponding Blasius flow profiles.

(1992), the non-parallel effects of the boundary layer decrease the critical R_L^* slightly. The observations in the present study are focused on the flow up to $x = 440$ mm, at which the x-Reynolds number R_x ($= xU_\infty/\nu$ where ν is the kinematic viscosity) is 1.2×10^5. The free-stream turbulence is about 0.3% of U_∞ at the tunnel exit and increases downstream up to the order of 1% beyond $x = 300$ mm. This increase is due to the upper and lower mixing layers developing from the nozzle exit. Even under such rather strong disturbances, the boundary layer remains completely laminar throughout the observation region at the present low Reynolds numbers. Without forcing, no evidence for the occurrence (beginning) of transition can be found in the observation region.

3. Excitation of hairpin eddies at the leading edge

First a description of how the spike stages can be realized near the leading edge is given. When the acoustic forcing is weak, only a viscosity-conditioned wave (i.e. the origin of a Tollmien–Schlichting (T–S) wave), superposed on the sound-induced Stokes layer, is generated near the leading edge. To show such leading-edge receptivity, figure 3 plots the x-distributions of u' (the r.m.s. value of the u-fluctuation) at $y = 0.5$ mm (near the wall) and 5 mm (outside the boundary layer) for the case of weak excitation. Here the frequency of the acoustic forcing f is 50 Hz, whose non-dimensional value $2\pi f\nu/U_\infty^2$ is 290×10^{-6}. The u' at $y = 5$ mm, i.e. the velocity component due to the radiated sound, accelerates around the sharp leading edge, and rapidly decreases in intensity downstream along the plate. Inside the boundary layer (at $y = 0.5$ mm), however, we can see some undulation in the x-distribution of u'. The wavelength of the undulation is 30–35 mm. This is no doubt due to the superposition of T–S waves arriving in and generated in the leading-edge region because the r.m.s. amplitude of the u-fluctuation consisting of the stationary forcing field (sound with wavelength 6.8 m) and the (superposed) relatively weak T–S wave should undergo such an undulation with the T–S wavelength as explained by Nishioka & Morkovin (1986; see their figure 4). Indeed, from the undulation wavelength (= 30–35 mm) and the frequency (50 Hz) the phase velocity of the superposed wave component is found to be about $0.4U_\infty$ ($= 1.6$ m s^{-1}), which corresponds to that of T–S wave. The superposed viscosity-

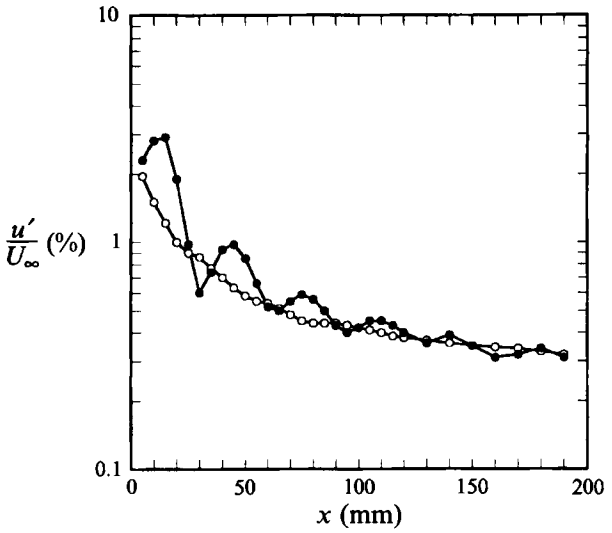

FIGURE 3. u' versus x for the case of weak forcing (at 50 Hz): ○, $y = 5$ mm; ●, $y = 0.6$ mm.

conditioned T–S wave decays quickly owing to a strong viscous effect near the leading edge, and the sound-induced Stokes layer alone is observed at the downstream station beyond $x = 100$ mm ($R_x = 2.8 \times 10^4$), as seen in figure 4 which compares the y-distributions of the amplitude and phase of the u-fluctuation (the forcing frequency component) observed at $x = 110$, 120, 130 and 140 mm, with the y-distributions of the theoretical Stokes layer (induced by the oscillating free stream); the phase $\theta(y)$ was measured by using a phase meter. The leading-edge receptivity mentioned is important for the appearance of T–S waves, but its detail is outside the scope of the present study which focuses on the subcritical transition.

On increasing the forcing, a local separation occurs at the leading edge as already mentioned. In terms of timescale, the separation bubble is less than one third of the period of the forcing (at 50 Hz) and importantly it accompanies an intense thin shear layer away from the wall. The thin bubble shear layer is quite unstable (to high-frequency disturbances) and soon breaks down into discrete vortices, which quickly (almost at the same time as the shear layer rolls up) evolve into hairpin-shaped vortices. So by adjusting the intensity of the acoustic forcing, we can observe flow stages, which, as far as the waveforms of u-fluctuation are concerned, are similar to the one-spike stage and the two-spike stage observed in the experiments on the ribbon-induced transition in Blasius flow (Klebanoff *et al.* 1962; Kovasznay *et al.* 1962) and in plane Poiseuille flow (Nishioka *et al.* 1980, 1981; Nishioka & Asai 1984). The one-spike stage and the two-spike stage thus realized near the leading edge are demonstrated in figure 5 in terms of the waveforms of the u-fluctuation at $x = 10$ mm. Figures 6(*a*) and 6(*b*) also illustrate these two stages in terms of the instantaneous equi-shear contours (i.e. $\partial(U+u)/\partial y =$ constant lines) at $x = 10$ and 30 mm, showing the formation of the bubble shear layer and its breakdown into discrete vortices which correspond to the high-frequency spikes in the waveforms of the u-fluctuation (figure 5): note that with the passage of hairpin eddies (high-frequency spikes), the near-wall flow is also highly disturbed. Here the flow is quite periodic near the leading edge, so we are able to obtain the instantaneous equi-shear contours by the periodic-sampling technique. We hereafter call these two flows the one-spike flow and the two-spike flow respectively.

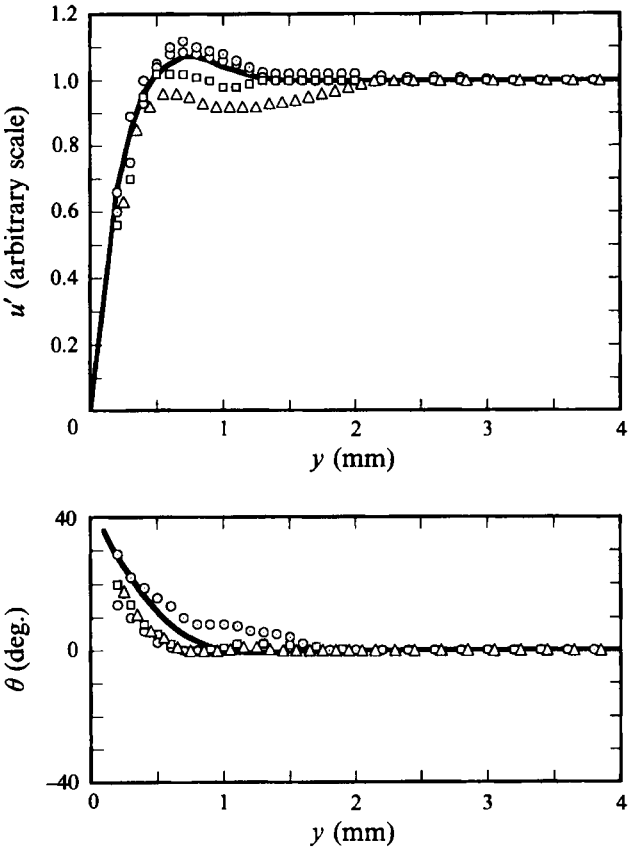

FIGURE 4. The y-distributions of amplitude u' and phase θ of the u-fluctuation at $x = 110$ mm (⊙), 120 mm (□), 130 mm (△) and 140 mm (○). Solid curves represent the corresponding distributions of the oscillating Stokes layer.

To see the three-dimensional structure of the excited vortices, figures 7(*a*) and 7(*b*) respectively show the plan view and cross-section view of smoke in the one-spike flow (corresponding to figure 5*a*). These pictures are taken not simultaneously but with the stroboscopic light being synchronized with the forcing signal so as to obtain the flow pattern at the same phase instance of the periodic forcing; the flow near the leading edge is almost periodic in time. The figure clearly shows the hairpin-shaped vortices resulting from the breakdown of the leading-edge bubble shear layer. Here the periodicity in the spanwise array of hairpin eddies is due to thin plastic tapes (0.05 mm thick) glued around the leading edge (every 6 mm in the z-direction) as mentioned earlier. Without the leading-edge tapes, the spacing changes in the spanwise direction and varies in the range from 4 to 7 mm. In the one-spike flow, a single hairpin eddy appears in each cycle of the periodic forcing between the neighbouring tapes, while in the two-spike flow, hairpin eddies are generated not only between the tapes but also directly behind each tape as seen in the plan view of the smoke-wire visualization in the two-spike flow, figure 7(*c*). The equi-shear contours in figures 6(*a*) and 6(*b*) are obtained at the z-position between the tapes.

Figure 7(*d*) shows the visualization picture when the forcing is increased much more (larger than that of the two-spike flow by about 25% in terms of the u-fluctuation due to the radiated sound). The separation bubble appears for at most one

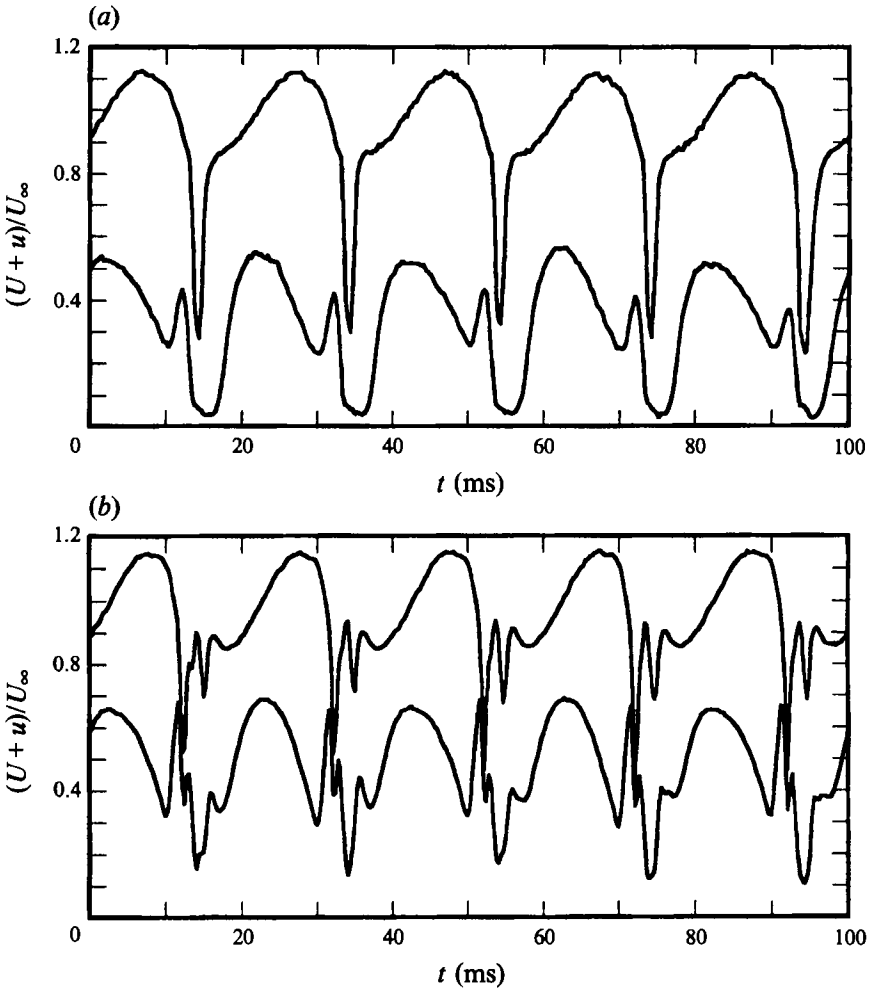

FIGURE 5. Waveforms of the u-fluctuation in the one-spike flow (a) and the two-spike flow (b). $y = 1.1$ mm (upper trace) and 0.3 mm (lower trace) in (a), $y = 1.6$ mm (upper) and 0.35 mm (lower) in (b).

third of the period of the forcing signal, so the number of spikes or hairpin eddies (whose frequency is about 400 Hz) in one cycle is not increased by more than two even under strong forcing (at the present frequency 50 Hz). However, for stronger forcing, the hairpin eddies excited can get more energetic because the bubble shear layer is much further away from the wall and the vortices evolving from it tend to be more free of the viscous wall effect. This is understood from the comparison of the y-distributions of u' at $x = 10$ mm for these three cases, shown in figure 8. Although the maximum r.m.s. values, u'_m, are almost the same, the y-position of the r.m.s. maximum becomes higher and moreover the total disturbance energy is apparently larger with increasing the forcing. In the next section, we examine the response of the boundary layer to the hairpin-shaped vortices excited in these cases to show the possibility of the subcritical transition and the related critical condition.

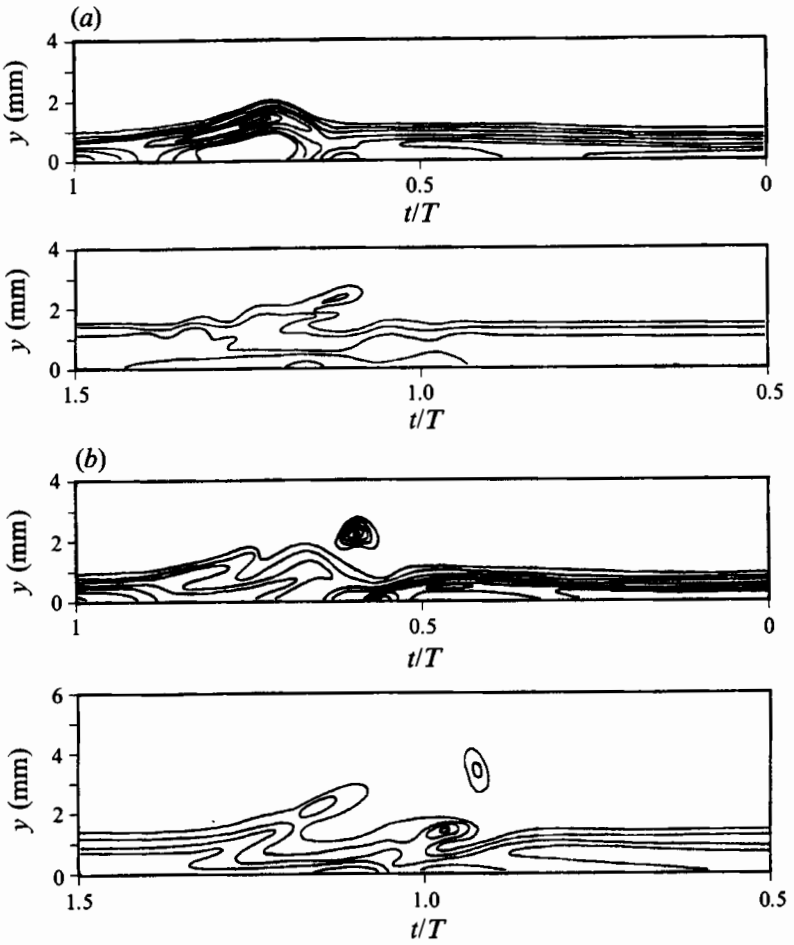

FIGURE 6. Equi-shear contours at $x = 10$ mm (upper) and $x = 30$ mm (lower) for (*a*) the one-spike flow, (*b*) the two-spike flow.

4. Disturbance growth at subcritical Reynolds numbers

As seen in figure 4, the instantaneous u-fluctuation induced by the hairpin eddies is more than 50% of U_∞ near the leading edge and thus quite large. However, the leading-edge-generated hairpin eddies (which we call the leading-edge hairpins for short) evolving from the thin bubble shear layer are so small in scale (their frequency is about 400 Hz) that they rapidly decay downstream due to viscous dissipation and diffusion. In terms of the waveform of the u-fluctuation, i.e. the high-frequency spikes, figure 9 demonstrates the decay of the leading-edge hairpins in the one-spike flow where a single hairpin eddy appears immediately downstream of the leading edge in each cycle of the acoustic forcing. The intensity decreases to one third from $x = 10$ to 40 mm, and we see only a faint remnant of the leading-edge hairpins beyond $x = 100$ mm. In this case, we observed that after the leading-edge hairpins decay, Blasius flow appears again together with the weak (two-dimensional) T–S wave. However, on increasing the forcing, the leading-edge hairpins become more energetic. Therefore they can survive further downstream and trigger the subcritical transition. To show this, figure 10 compares the flow developments in the three cases, i.e. the one-spike

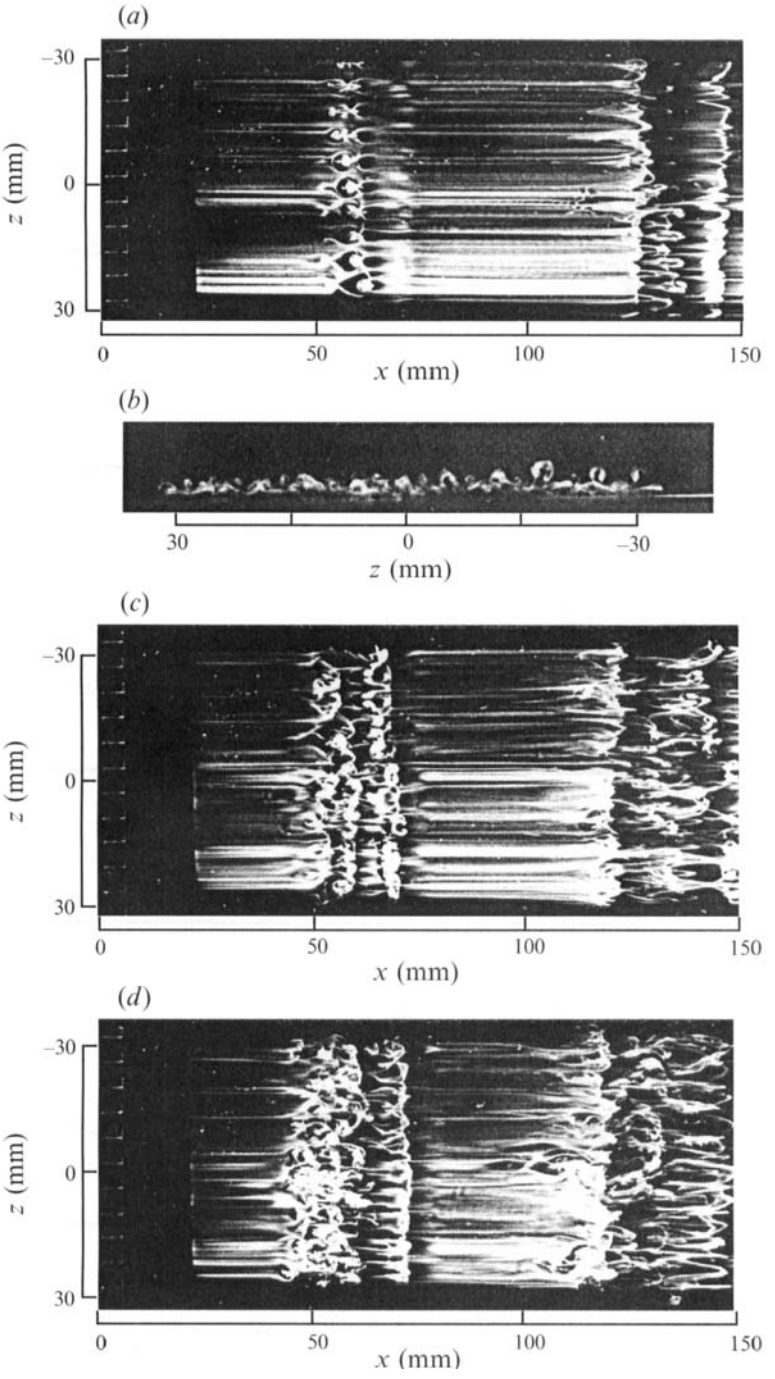

FIGURE 7. Smoke-wire visualization of the leading-edge-generated hairpin eddies: (*a*, *b*) the one-spike flow (plan and cross-section view), (*c*) the two-spike flow, (*d*) the energetic two-spike flow. The smoke wire is set at $(x, y) = (25, 2.5$ mm) in the plan view, and at $(x, y) = (20, 0.5$ mm) in the cross-section view ($x = 55$ mm) in (*b*).

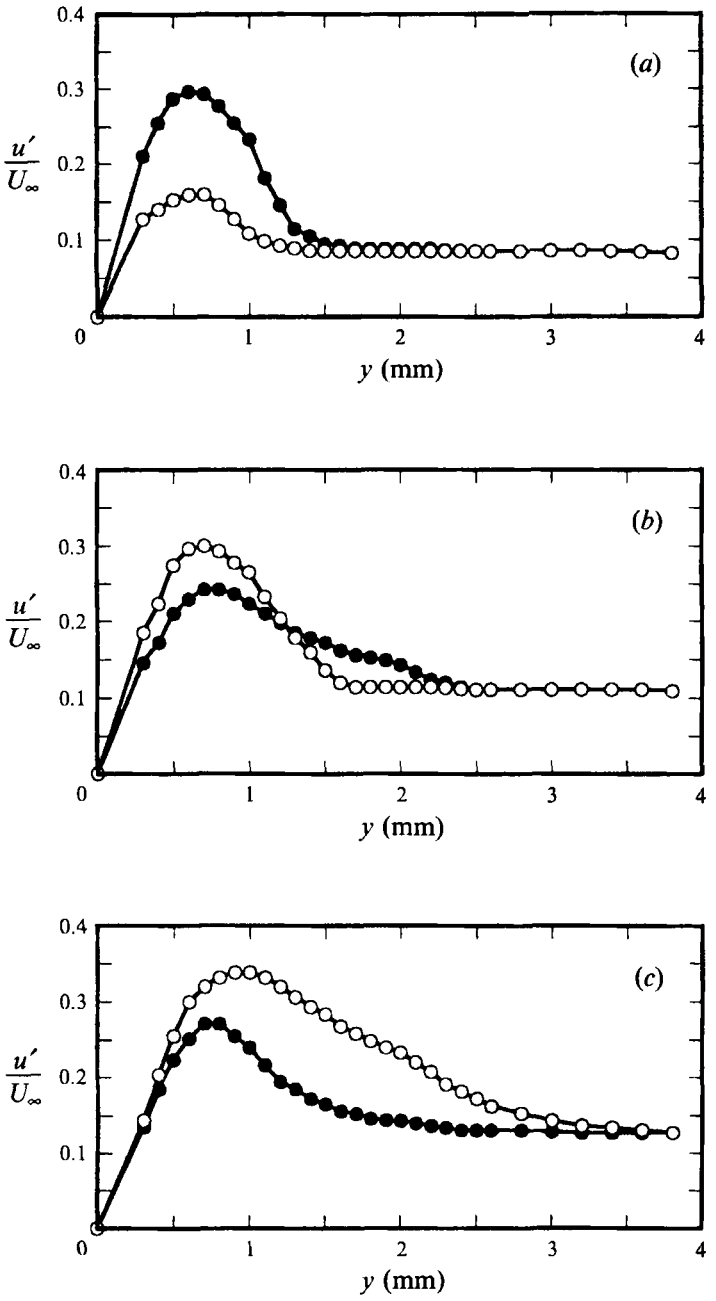

FIGURE 8. Comparison of the r.m.s. intensity of the u-fluctuation u' at $x = 10$ mm. (*a*) the one-spike flow, (*b*) the two-spike flow and (*c*) the energetic two-spike flow. ●, at a z-position between neighbouring tapes; ○, directly behind tape.

flow, the two-spike flow and the two-spike flow with more energetic leading-edge hairpins (which we call the energetic two-spike flow), using side view pictures of smoke-wire visualization. In the two-spike flow, we see only the leading-edge hairpins in the whole observation region (up to $x = 300$ mm) as in the one-spike flow, while in the energetic two-spike flow we can see that successive growth of vortices occurs

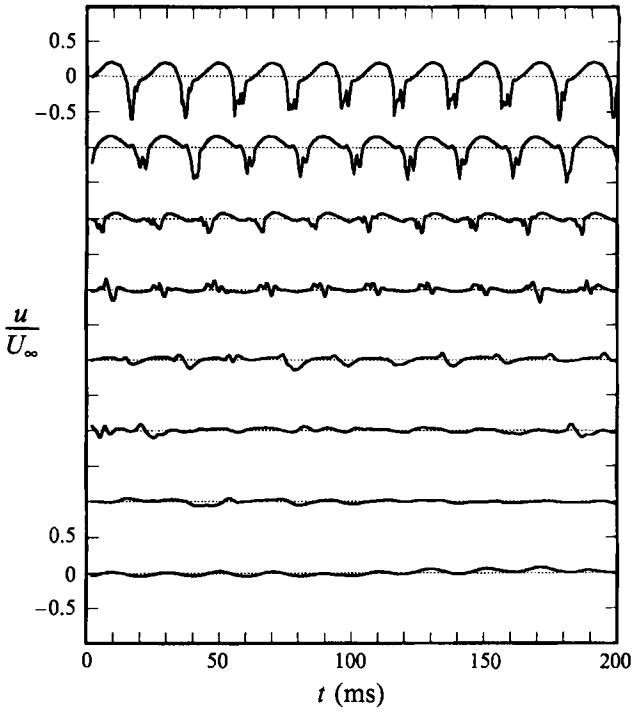

FIGURE 9. Waveforms of the u-fluctuation (at $y = 1$ mm) in the one-spike flow. From top to bottom, $x = 10$, 20, 30, 40, 60, 80, 120 and 160 mm.

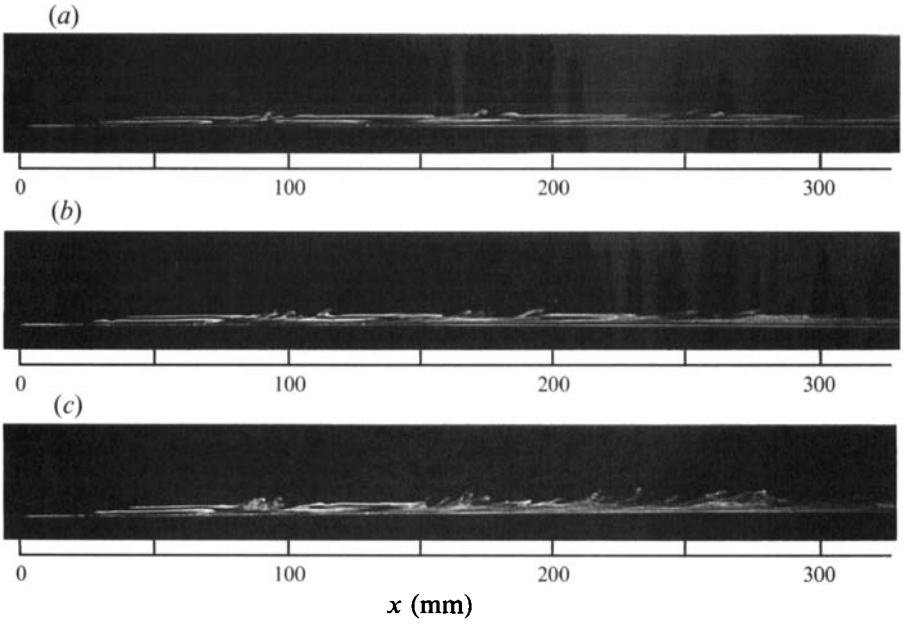

FIGURE 10. Smoke-wire visualizations of the one-spike flow (*a*), the two-spike flow (*b*) and the energetic two-spike flow (*c*). Stroboscopic light illuminates only a spanwise width of about 10 mm for these side-view pictures. Two smoke wires are set at $(x, y) = (25, 0.5$ mm) and (35, 2.5 mm).

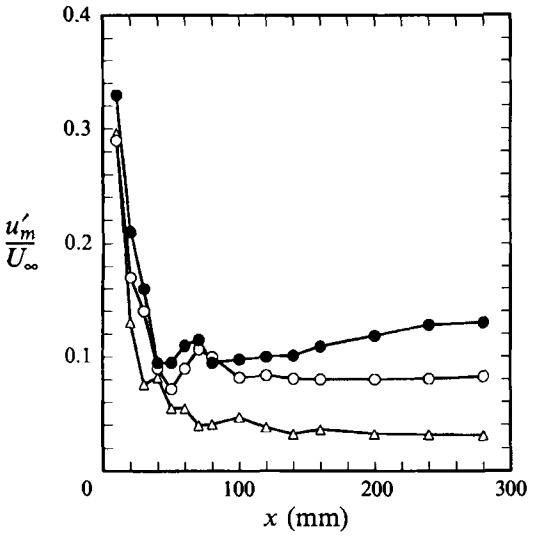

FIGURE 11. Comparison of the development of u'_m among the one-spike flow (△), the two-spike flow (○) and the energetic two-spike flow (●).

beyond $x = 180$ mm to lead to wall turbulence. These pictures clearly indicate the presence of the critical condition for the disturbance growth leading to the subcritical transition, and it will be examined below in detail.

Figure 11 compares the development of the u-fluctuation in the one-spike, the two-spike and the energetic two-spike flows by plotting the maximum r.m.s. value u'_m/U_∞ against x. In all the cases, the u-fluctuation quickly decays until levelling off at around $x = 100$ mm ($R_x = 2.8 \times 10^4$) except for the wiggle around $x = 60$ mm; the wiggle is mainly due to the superposed sound. However, in the energetic two-spike flow, after levelling at a value of 10%, u'_m/U_∞ then starts to grow beyond $x = 140$ mm ($R_x = 3.9 \times 10^4$). In the two-spike flow, u'_m/U_∞ decays down to about 8% at around $x = 100$ mm, and never starts to grow downstream in the subcritical region up to $x = 300$ mm ($R_x = 8.3 \times 10^4$), where R_L^* is about 500, nearly at the critical for the linear instability. Thus the subcritical transition occurs only when u'_m/U_∞ (mainly due to the disturbing leading-edge hairpins) is greater than the threshold of about 10%. Of course, the intensity of the instantaneous u-fluctuation might be more important because around the critical station the hairpin eddies do not yet cover the whole period in time. So figure 12 illustrates the waveforms of the u-fluctuation at the critical station in the energetic two-spike flow. The instantaneous u-fluctuation is as large as 20–30% of U_∞ which is of almost the same order as that observed in the developed turbulent boundary layer.

Then how does the disturbance growth occur? Up to $x = 100$ mm, the leading-edge hairpins are very active and can lift up the near-wall fluid both in the two-spike flow and the energetic two-spike flow. Beyond $x = 100$ mm, however, the leading-edge hairpins become weak and no remarkable near-wall activity is observed in the two-spike flow. On the other hand, figure 13(*a*, *b*) visualizes the flow development around the critical station in the energetic two-spike flow in detail. The smoke is released from two y-positions, i.e. at the boundary-layer edge and near the wall (similar to the visualization in figure 10) to give information on the decay of the leading-edge hairpins as well as the associated near-wall activity. As seen in the figure, the leading-edge hairpins are still active beyond $x = 100$ mm in the energetic two-spike flow.

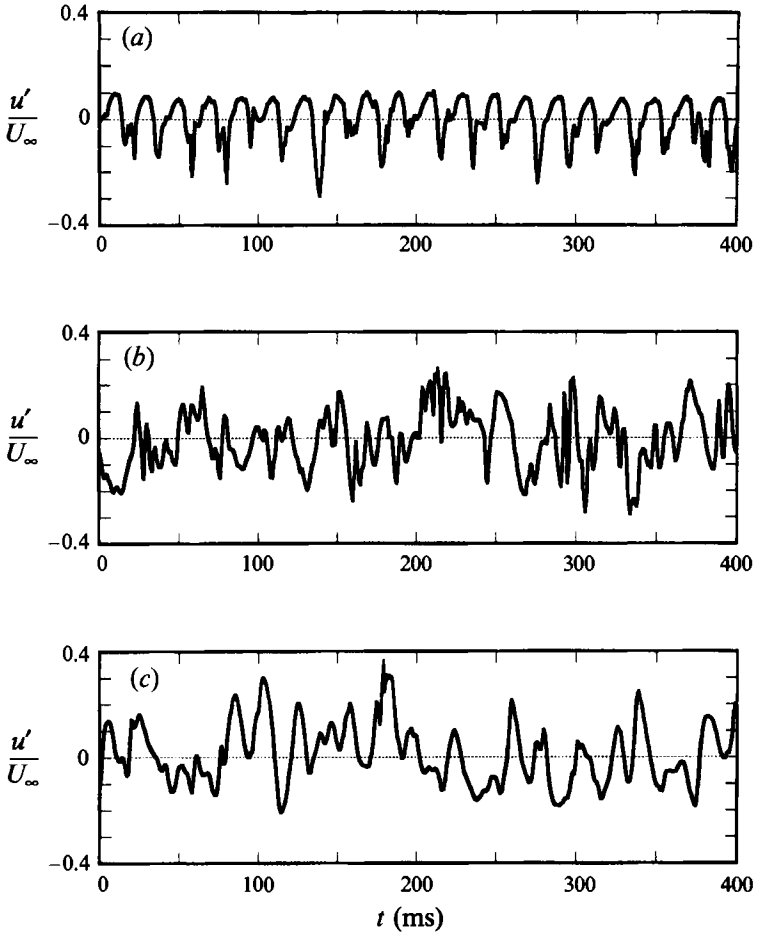

FIGURE 12. Waveforms of the u-fluctuation at $x = 140$ mm for the energetic two-spike flow. (a) $y = 3.8$ mm, (b) 1.5 mm and (c) 0.9 mm.

Importantly, the lifted-up smoke released from $x = 90$ mm shows that, associated with the passage of the leading-edge hairpins, the shear layer near the wall starts to develop into discrete vortices at around $x = 150$ mm. Indeed, the cross-section view of the near-wall flow given in figure 13(b), taken at an instant half a period after the passage of the heads of the leading-edge hairpins (visualized in figure 13a), indicates the appearance of many mushrooms, which no doubt shows the development of three-dimensional wall shear layers with streamwise vortices. They evolve into hairpin eddies downstream, which we call 'wall hairpins' (Asai & Nishioka 1990). Beyond $x = 200$ mm, the plan view of a smoke-wire visualization, figure 14(a), shows no laminar region over the whole spanwise extent, which results from the break-up of the wall shear layers into hairpin eddies as seen in the side-view picture, figure 14(b). In this regard, Smith and his colleagues (Smith *et al.* 1991; Haidari & Smith 1994) examined the regeneration process of hairpin vortices in detail through exciting single hairpin vortices by means of controlled injection of wall fluid through a streamwise slot, and revealed that secondary hairpin vortices (wall hairpins in our case) are generated between the legs of the primary hairpins (corresponding to the leading-edge hairpins) as well as directly behind each leg through a process of vortex–surface interaction. They proposed that

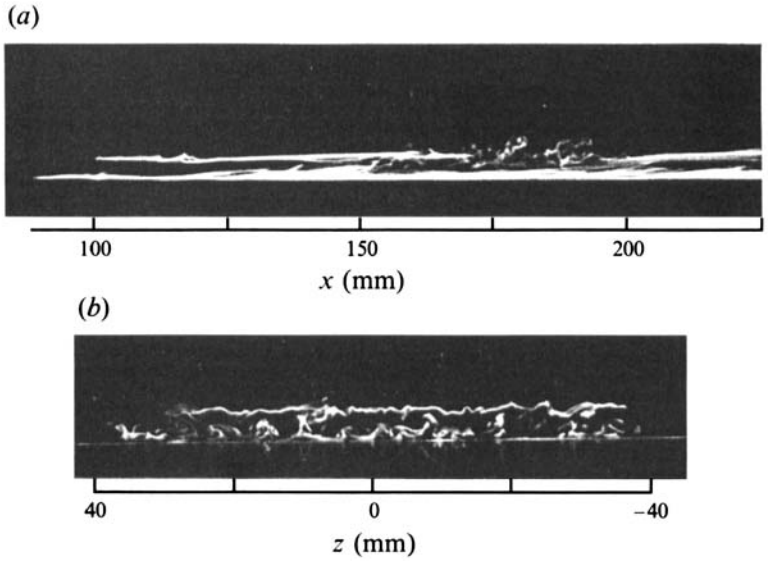

FIGURE 13. Smoke-wire visualization of the energetic two-spike flow: (*a*) side view, (*b*) cross-section view (at $x = 150$ mm). Two smoke wires are set at $(x, y) = (90, 0.5$ mm) and (100, 3.5 mm).

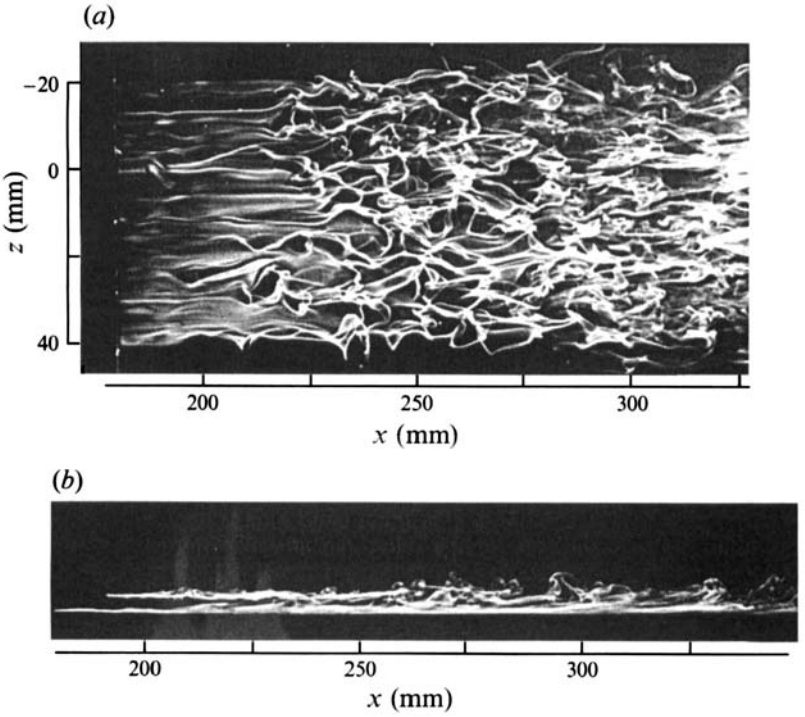

FIGURE 14. Smoke-wire visualization of the energetic two-spike flow: (*a*) plan view, (*b*) side view. A smoke-wire is set at $(x, y) = (180, 3.5$ mm) in (*a*), and two smoke wires are set at $(x, y) = (180,$ 0.5 mm) and (190, 4.0 mm) in (*b*).

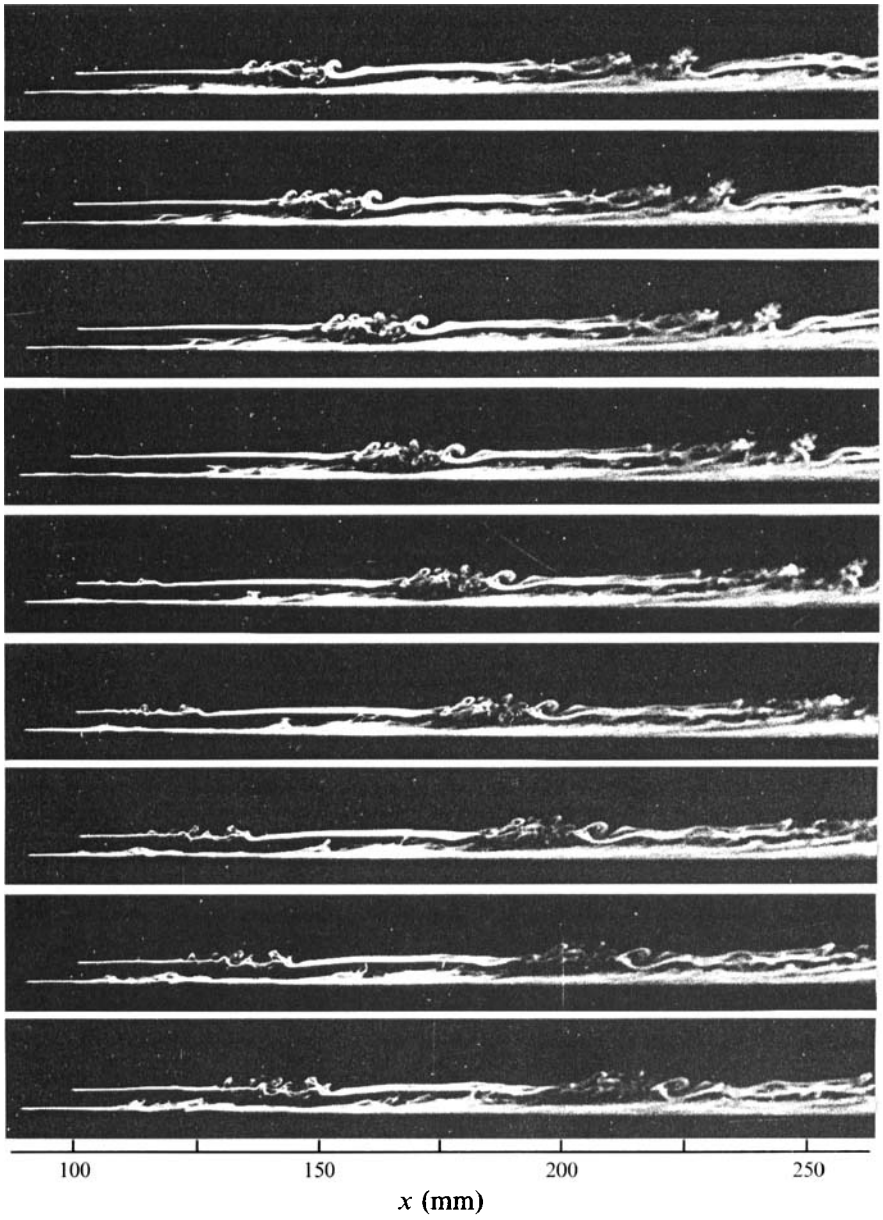

FIGURE 15. Regeneration of hairpin eddies beyond the critical station, illustrated by a sequence of side-view pictures taken with high-speed camera. Time interval is 2.5 ms between frames. Two smoke wires are set at $(x, y) = (90, 0.5\text{ mm})$ and $(100, 3.5\text{ mm})$.

the adverse pressure gradient imposed by the primary hairpins causes the eruption (lift-up) of low-speed fluid leading to the formation of secondary hairpins. In our case too, the successive growth of the wall shear layer (lifted up by leading-edge hairpins) into wall hairpins starts to occur before being caught up by the leading-edge hairpins (of the next cycle) coming from upstream, suggesting a local instability of the disturbed wall shear layer itself. It should be noted that the heads of the leading-edge hairpins move at a speed of about $0.9U_\infty$, while the near-wall eddies move at $0.5U_\infty$ to $0.6U_\infty$. Such an

instability responsible for the regeneration of wall hairpins has to occur within the viscous diffusion time as discussed below.

In order to analyse the growth (or regeneration) of wall hairpins, a time sequence of the flow development around the critical station in the energetic two-spike flow is visualized in figure 15 by using a high-speed camera system. The photos are taken at intervals of 1/400 s, one eighth of the period of the acoustic forcing, and nine frames from top to bottom complete one whole cycle of the forcing (at 50 Hz). Observe the near-wall smoke released from $y = 0.5$ mm (at the height of the momentum thickness). Soon after the passage of the leading-edge hairpins, the near-wall smoke is lifted up to the boundary-layer edge ($y \approx 4$ mm) within a time interval of about 5/400 s (5 frames), which gives us a rough estimation of the v-fluctuation associated with the near-wall activity, namely about the order of 5% of U_∞ or more. As seen from the cross-section view (figure 13*b*), the v-fluctuation is caused by the near-wall streamwise vortices (probably induced by hairpin eddies coming from upstream and/or their legs themselves). So, if the streamwise vortices are active, the wall shear layer is lifted up away from the wall, and simultaneously is stretched in the lateral (spanwise) direction. The resulting intense wall shear layer is free from the wall effect and may become unstable. For the regeneration of wall hairpins, however, such a wall shear layer (with streamwise vortices) has to break down before decaying due to the effects of viscous diffusion and dissipation. In the present case, the timescale required for the generation of wall hairpins is 5/400 s, which is of the same order as the viscous diffusion time θ^2/ν (≈ 17 ms) around the critical station when we take the momentum thickness θ (about 0.5 mm) as the measure of wall-shear-layer thickness. Thus, the v-fluctuation (5% of U_∞) is really the critical intensity for the growth or regeneration of wall hairpins. We also made a similar analysis of visualization data in the two-spike flow where the near-wall flow is not active even beyond the above-mentioned critical station, and found that the intensity of the v-fluctuation has already decreased down to 1% of U_∞ beyond $x = 100$ mm. With these observations, the present critical intensity of the v-fluctuation may be written as $v\theta/\nu > 8$, since $\delta/\theta \approx 8$ for Blasius flow.

5. Development of wall turbulence structure

As observed in the preceding section, the successive generation (or regeneration) of hairpin eddies is responsible for the occurrence of subcritical transition. In order to further clarify the critical Reynolds number for the occurrence of the subcritical transition, we measure the coefficient of local skin friction, C_f', at various x-stations. Here C_f' is obtained from the mean velocity distribution $U(y)$ (and $\partial U/\partial y$ at the wall) at each x-station. Thus, the hot-wire probe is carefully traversed towards the wall to as close as possible: the thickness of the viscous sublayer is about 0.5 mm at $x = 440$ mm. Also note that for each y-traverse, the wall position ($y = 0$) is precisely determined by measuring the laminar Blasius flow profile at each x-station without the forcing. The result is plotted against the x-Reynolds number R_x in figure 16. C_f' starts to deviate from the laminar value at around $R_x = 2.8 \times 10^4$ ($x = 100$ mm) and increases beyond $R_x = 3.9 \times 10^4$ ($x = 140$ mm) to approach that of the wall turbulence downstream. This x-station ($R_x = 3.9 \times 10^4$) corresponds to the critical station for u_m' to start to increase downstream. Indeed, it is after the appearance and growth of wall hairpins (mushrooms in the cross-section smoke view) that the local skin friction C_f' starts to increase downstream. This indicates an important role of wall hairpins in the momentum transfer towards the wall: this has also been found in our previous experiment on the ribbon-induced transition (Nishioka *et al.* 1980; Nishioka & Asai

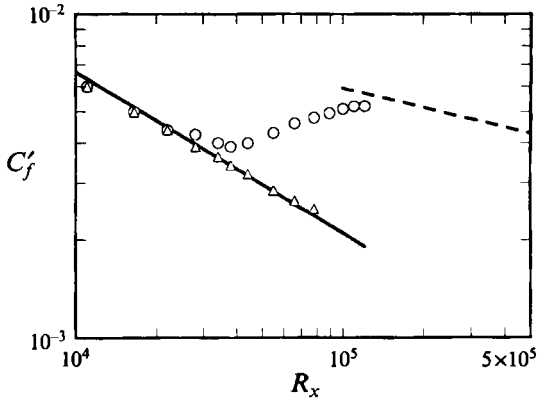

FIGURE 16. Local skin friction C_f' versus R_x: ○, energetic two-spike flow; △, undisturbed flow without acoustic forcing; ——, Blasius flow; – – –, developed turbulent flow (Prandtl).

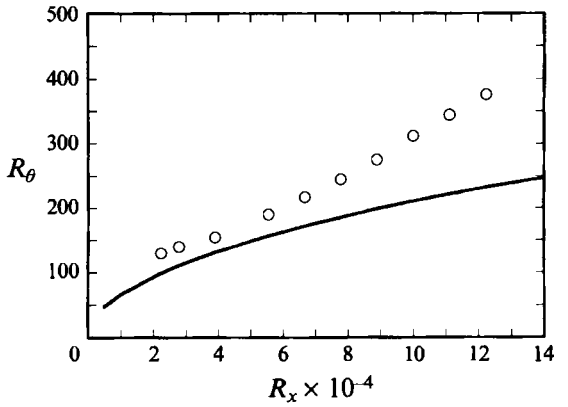

FIGURE 17. Momentum thickness Reynolds number R_θ versus R_x. Solid curve represents $R_{\theta L}$ for undisturbed Blasius flow.

1984). In the present experiment on the subcritical boundary-layer transition, it should be noted that according to the hot-wire signals as well as a number of visualization photographs, the near-wall activity is slightly intermittent around the critical station even in the energetic two-spike flow.

Figure 17 plots the momentum-thickness Reynolds number R_θ against R_x in the energetic two-spike flow, where the momentum thickness θ is calculated from the y-distribution of time-mean velocity $U(y)$ at each x-station. Owing to the generation of the vortices at the leading edge, the momentum thickness is slightly larger than that of the undisturbed Blasius flow (represented by the solid curve) even at the x-stations below the critical: R_θ is greater than $R_{\theta L}$ by 20–25 at the x-stations below $R_x = 3.9 \times 10^4$. Even in terms of R_θ, the transition Reynolds number (≈ 150) is less than the critical value calculated from the Orr–Sommerfeld stability equation, $R_{\theta L} = 200$. Here it is also worth noting that the critical R_θ found in the present experiment is very close to the minimum transition R_θ (≈ 130) obtained in plane Poiseuille flow under highly disturbed inlet flow conditions (Nishioka & Asai 1985). The stability characteristics of the linear instability (including the critical Reynolds number) are very sensitive to the velocity distribution of the basic flow $U(y)$; see, for

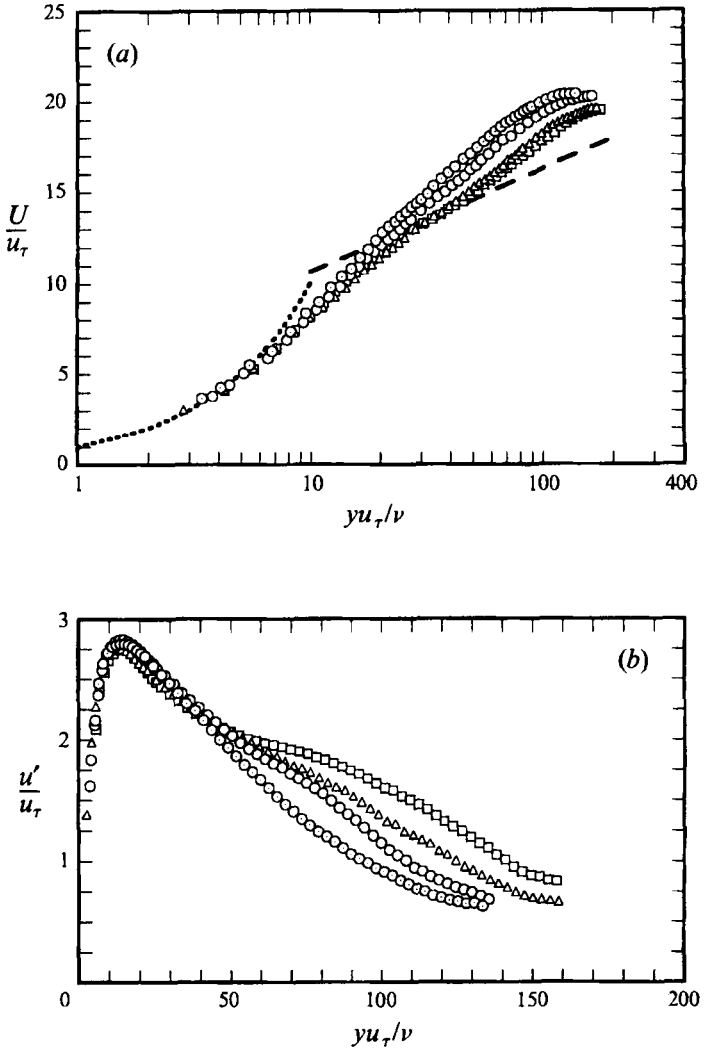

FIGURE 18. The y-distributions of time-mean velocity U in (a) and r.m.s. intensity u' in (b): ⊙, $R_x = 8.9\times10^4$; ○, $R_x = 1.0\times10^5$; △, $R_x = 1.1\times10^5$; □, $R_x = 1.2\times10^5$; ---, $U/u_\tau = 5.62\log(yu_\tau/\nu)+5.0$; ·····, $U/u_\tau = yu_\tau/\nu$.

instance, Drazin & Reid (1981, figure 4.24). On the other hand, the disturbance growth in the present subcritical transition is due to the break-up of the local wall shear layer generated by the primary hairpin eddies (in particular, their legs) so that the thickness of the wall shear layer is of vital importance for the onset of the transition. Therefore, considering that the momentum thickness is a measure of wall shear layer thickness, the coincidence of the minimum transition R_θ for Blasius flow and plane Poiseuille flow seems to be quite reasonable.

Figure 18 shows the development of wall turbulence structure in terms of $U(y)$ and $u'(y)$ at $R_x = 0.89\times10^5$, 1.0×10^5, 1.1×10^5 and 1.2×10^5 ($x = 320$, 360, 400 and 440 mm) where the C_f' approaches that of the wall turbulence. All the quantities are non-dimensionalized with the local friction velocity u_τ and the kinematic viscosity ν. The y-distributions of u' near the wall are similar to each other at these four stations with a maximum at $yu_\tau/\nu = 15$ (that for developed wall turbulence), and thus it seems

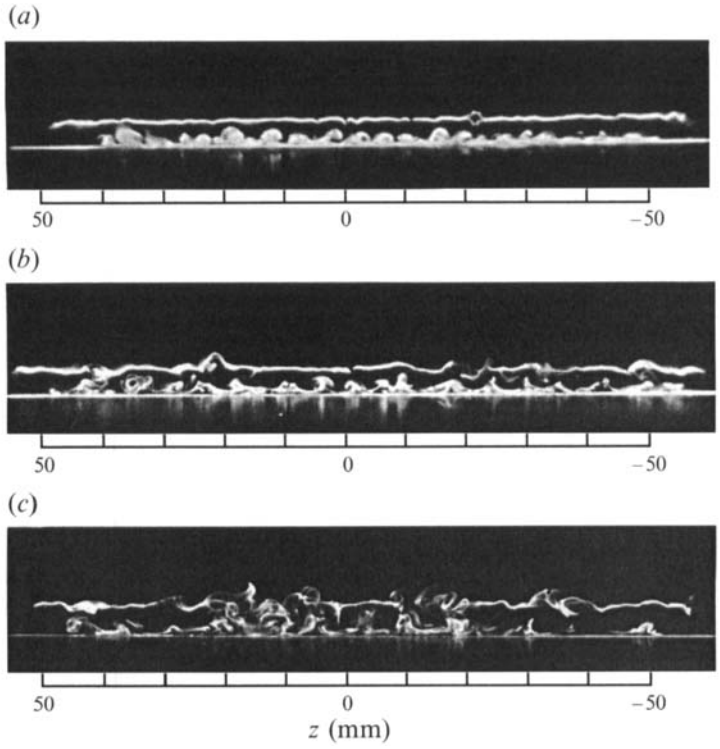

FIGURE 19. Cross-section view of near-wall flow. (*a*) $x = 110$ mm ($R_x = 3.1 \times 10^4$), (*b*) $x = 200$ mm ($R_x = 5.6 \times 10^4$), (*c*) $x = 320$ mm ($R_x = 8.9 \times 10^4$).

that the wall turbulence structure has already been established near the wall at these stations. As R_x increases from 0.89×10^5 to 1.2×10^5, the turbulent region extends to the larger y-region. However, it is beyond $R_x = 1.1 \times 10^5$ (about 350 in terms of R_θ) that the y-distribution of U/u_τ starts to exhibit a log-law (Coles & Hirst 1968). Even at $R_x = 1.2 \times 10^5$, the log-law region is only limited and the wall region is overlapped by the outer intermittent region.

We show another important result on the development of the wall turbulence structure in this transition in figure 19 which compares the visualization pictures at three cross-sections, $x = 110$, 200 and 320 mm ($R_x = 3.1 \times 10^4$, 5.6×10^4 and 8.9×10^4). In each photo, the smoke was released from the x-station 50 mm upstream of the observation x to visualize active vortical structures at each station. We can see a continual development of the mushrooms (caused by a pair of counter-rotating streamwise vortices) with increasing their spanwise scale. The active mushrooms reach the boundary-layer edge within the distance of 50 mm (about 10 times the boundary-layer thickness). These correspond to the lifted-up wall hairpins seen in the side-view picture, figure 14(*b*). Thus, together with the corresponding side-view pictures, these visualizations reveal that the successive evolution of wall shear layers into wall hairpins can lead to wall turbulence. Even at $x = 320$ mm where the flow starts to exhibit the wall turbulence structure, distinct mushrooms moving towards the boundary layer edge are regularly aligned, with a spanwise spacing of 5–10 mm, though most of the lifted smoke (caused by streamwise vortices) is skewed or asymmetric. From these visualization data, we measure the spanwise spacing of mushrooms (or lifted-up smoke associated with streamwise vortices) λ at various x-stations and obtain its histogram as

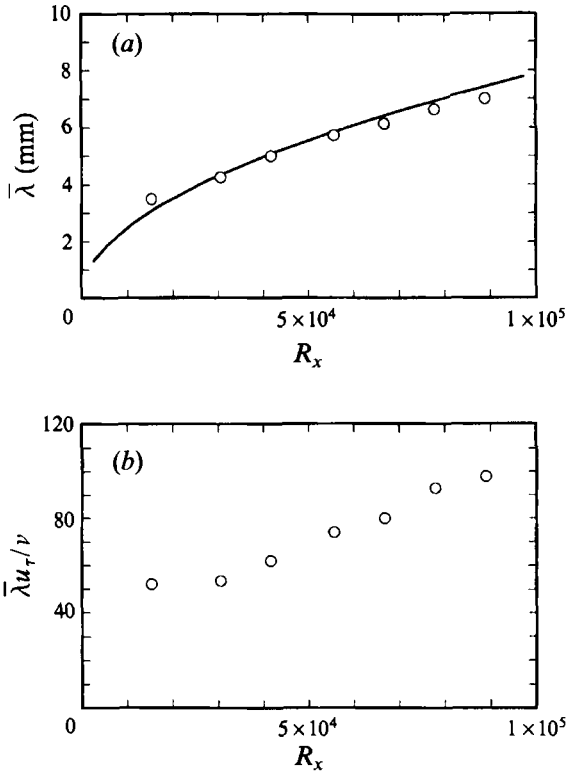

FIGURE 20. Development of mean spanwise spacing $\bar{\lambda}$. (*a*) $\bar{\lambda}$ versus R_x, (*b*) $\bar{\lambda}u_\tau/\nu$ versus R_x. ——; $\bar{\lambda} \propto (\nu x/U_\infty)^{1/2}$.

well as the mean value $\bar{\lambda}$; the number of sample data points is more than 200. Figure 20(*a*) plots the mean value $\bar{\lambda}$ against R_x, showing that the spacing $\bar{\lambda}$ is as small as 3 mm (i.e. half the spacing of the leading-edge tapes) near the leading edge and increases up to about 7 mm through the transition process. The downstream increase of $\bar{\lambda}$ seems to be well correlated with the growth of the laminar (Blasius) boundary layer due to viscous diffusion (represented by the solid curve), i.e. $\bar{\lambda} \propto (\nu x/U_\infty)^{1/2}$, in particular around the critical station. When we measure the spacing in local wall units, however, $\bar{\lambda}$ tends to approach a constant value at the downstream station, as shown in figure 20(*b*). Up to the critical station ($R_x = 3.9\times10^4$), $\bar{\lambda}$ remains at about $50\nu/u_\tau$, half the well-known mean spacing of the wall streaks in developed wall turbulence, so that initially the wall shear layers are strongly influenced by viscosity. Beyond the critical station where the near-wall flow becomes active, $\bar{\lambda}$ increases up to the asymptotic value of $100\nu/u_\tau$ beyond $R_x = 8.9\times10^4$. Here, we of course have to understand that the smoke patterns do not exactly correspond to the vortical structures at the observation x and the spacing λ measured from the cross-section view might be slightly smaller than the real spacing at each station owing to time history of the smoke, However, the result clearly indicates that the wall shear layers themselves successively grow, increasing in scale, and finally evolve into hairpin eddies and/or streamwise vortices of the characteristic scale typical for the developed wall turbulence, i.e. $\bar{\lambda}u_\tau/\nu = 100$.

6. Concluding remarks

In the present study, we have examined the subcritical transition triggered by energetic hairpin eddies. Even in the presence of highly disturbing hairpin eddies, the boundary layer is found to be stable below the x-Reynolds number $R_x = 2.8 \times 10^4$ in the sense that no active growth of the disturbed wall shear layers occurs. On the other hand, beyond $R_x = 3.9 \times 10^4$, the wall shear layers with streamwise vortices, which appear after the passage of the leading-edge generated hairpin eddies, become active and themselves evolve into hairpin eddies in succession. Correspondingly, the local skin friction C_f' increases beyond $R_x = 3.9 \times 10^4$. The modification of the mean flow U due to the vortex excitation is not large below $R_x = 3.9 \times 10^4$ in terms of the difference between $R_{\theta L}$ and R_θ: for instance, $R_{\theta L}$ and R_θ are respectively 127 and 150 at $R_x = 3.9 \times 10^4$. So, we may surely say that the transition in the Blasius boundary layer really occurs at the subcritical Reynolds numbers. In terms of u- and v-fluctuations, the intensity of the near-wall activity triggering the growth of the wall shear layer around the critical station mentioned above is almost the same as that of fully turbulent cases. The critical intensity of the v-fluctuation may be written as $v\theta/\nu = 8$. The momentum-thickness Reynolds number R_θ is about 150 ($R_{\theta L} = 127$ for Blasius flow) at the critical station for the regeneration of hairpin eddies mentioned above, and 350 for the appearance of a log-law velocity distribution (at $R_x = 1.1 \times 10^5$).

The successive growth of wall hairpins is probably due to an inflectional instability of the three-dimensional wall shear layer lifted up by the streamwise vortices which are the legs of hairpin eddies or the secondary vortices induced by them, though the development of the wall shear layer with streamwise vortices is strongly influenced by viscosity at the subcritical Reynolds numbers. Indeed, the growth of the wall shear layer is highly dependent on the intensity of the disturbing hairpin eddies. It is also found that beyond the critical station, the spanwise scale of the active wall shear layers in wall units is increased downstream, finally reaching $\bar{\lambda}u_\tau/\nu = 100$ (beyond $R_x = 8.9 \times 10^4$) in terms of the mean spanwise distance between the neighbouring ejection ($\bar{\lambda}$). On the basis of the present results for the subcritical transition in Blasius flow, we may say that the regeneration of wall hairpins can generate and sustain wall turbulence.

The authors wish to express their cordial thanks to Professors S. Iida and H. Sato for their continual encouragement. This work was in part supported by a Grant-in-Aid for Scientific Research (No. 06651070), the Ministry of Education, Science and Culture, Japan.

REFERENCES

ACARLAR, M. S. & SMITH, C. R. 1987*a* A study of hairpin vortices in a laminar boundary layer. Part 1. Hairpin vortices generated by a hemisphere protuberance. *J. Fluid Mech.* **175**, 1–41.

ACARLAR, M. S. & SMITH, C. R. 1987*b* A study of hairpin vortices in a laminar boundary layer. Part 2. Hairpin vortices generated by fluid injection. *J. Fluid Mech.* **175**, 43–83.

ASAI, M. & NISHIOKA, M. 1989 Origin of the peak–valley wave structure leading to wall turbulence. *J. Fluid Mech.* **208**, 1–23.

ASAI, M. & NISHIOKA, M. 1990 Development of wall turbulence in Blasius flow. In *Laminar-Turbulent Transition* (ed. D. Arnal & R. Michel), pp. 215–224. Springer.

BAYLY, B. J., ORSZAG, S. A. & HERBERT, TH. 1988 Instability mechanisms of boundary layer transition. *Ann. Rev. Fluid Mech.* **20**, 359–391.

BERTOLOTTI, F. P., HERBERT, TH. & SPALART, P. R. 1992 Linear and nonlinear stability of the Blasius boundary layer. *J. Fluid Mech.* **242**, 441–474.

CARLSON, D. R., WIDNALL, S. E. & PEETERS, M. E. 1982 A flow visualization of transition in plane Poiseuille flow. *J. Fluid Mech.* **121**, 487–505.

COLES, D. D. & HIRST, E. A. (Eds.) 1968 *Proc. AFOSR-IFP-Stanford Conf. on Computation of Turbulent Boundary Layers, Stanford University.*

DRAZIN, P. G. & REID, W. H. 1981 *Hydrodynamic Stability*, pp. 211–239. Cambridge University Press.

FASEL, H. 1990 Numerical simulation of instability and transition in boundary layer flows. In *Laminar-Turbulent Transition* (ed. D. Arnal & R. Michel), pp. 587–598. Springer.

FASEL, H. & KONZELMAN, U. 1990 Non-parallel stability of a flat-plate boundary layer using the complete Navier–Stokes equations. *J. Fluid Mech.* **221**, 311–347.

GASTER, M. 1969 On the flow along swept leading edge. *Aero. Q.* **18**, 165–184.

HAIDARI, A. H. & SMITH, C. R. 1994 The generation and regeneration of single hairpin vortices. *J. Fluid Mech.* **277**, 135–162.

HAMA, F. R. & NUTANT, J. 1963 Detailed flow-field of transition process in a thick boundary layer. In *Proc. 1963 Heat Transfer and Fluid Mech. Inst., Stanford University*, pp. 77–93.

HENNINGSON, D. S. & ALFREDSSON, P. H. 1987 The wave structure of turbulent spots in plane Poiseuille flow. *J. Fluid Mech.* **178**, 405–421.

HENNINGSON, D. S. & KIM, J. 1991 On turbulent spots in plane Poiseuille flow. *J. Fluid Mech.* **228**, 183–205.

HERBERT, TH. 1988 Secondary instability of boundary layers. *Ann. Rev. Fluid Mech.* **20**, 487–526.

KACHANOV, YU. S. 1994 Physical mechanisms of laminar-boundary-layer transition. *Ann. Rev. Fluid Mech.* **26**, 411–482.

KLEBANOFF, P. S., TIDSTROM, K. D. & SARGENT, L. M. 1962 The three-dimensional nature of boundary layer instability. *J. Fluid Mech.* **12**, 1–34.

KLINGMANN, B. G. B. 1992 On transition due to three-dimensional disturbances in plane Poiseuille flow. *J. Fluid Mech.* **240**, 167–195.

KOVASZNAY, L. S. G., KOMODA, H. & VASUDEVA, B. R. 1962 Detailed flow field in transition. In *Proc. 1962 Heat Transfer and Fluid Mech. Inst., Stanford University*, pp. 1–26.

MATSUI, T. 1980 Visualization of turbulent spots in the boundary layer along a flat plate in a water flow. In *Laminar-Turbulent Transition* (ed. R. Eppler & H. Fasel), pp. 288–296. Springer.

MORKOVIN, M. V. 1988 Recent insights into instability and transition. *AIAA*-88-3675.

NISHIOKA, M. & ASAI, M. 1984 Evolution of Tollmien–Schlichting waves into wall turbulence. In *Turbulence and Chaotic Phenomena in Fluids* (ed. T. Tatsumi), pp. 87–92. North-Holland.

NISHIOKA, M. & ASAI, M. 1985 Some observations of the subcritical transition in plane Poiseuille flow. *J. Fluid Mech.* **150**, 441–450.

NISHIOKA, M., ASAI, M. & IIDA, S. 1980 An experimental investigation of the secondary instability. In *Laminar-Turbulent Transition* (ed. R. Eppler & H. Fasel), pp. 37–46. Springer.

NISHIOKA, M., ASAI, M. & IIDA, S. 1981 Wall phenomena in the final stage of transition to turbulence. In *Transition and Turbulence* (ed. R. E. Meyer), pp. 113–126. Academic.

NISHIOKA, M., IIDA, S. & ICHIKAWA, Y. 1975 An experimental investigation of the stability of plane Poiseuille flow. *J. Fluid Mech.* **72**, 731–751.

NISHIOKA, M. & MORKOVIN, M. V. 1986 Boundary-layer receptivity to unsteady pressure gradients: experiments and overview. *J. Fluid Mech.* **171**, 219–261.

ORSZAG, S. A. 1971 Accurate solution of the Orr–Sommerfeld stability equation. *J. Fluid Mech.* **50**, 689–703.

POLL, D. I. A. 1979 Transition in the infinite swept attachment line boundary layer. *Aero. Q.* **30**, 607–629.

SANDHAM, N. D. & KLEISER, L. 1992 The late stages of transition to turbulence in channel flow. *J. Fluid Mech.* **245**, 319–348.

SMITH, C. R., WALKER, J. D. A., HAIDARI, A. H. & SOBRUN, U. 1991 On the dynamics of near-wall turbulence. *Phil. Trans. R. Soc. Lond.* A **336**, 131–175.